**This is the Pre-Published Version.**

This is the accepted version of the publication Li, Y., Wang, K., Wang, Q., Yang, J., Zhou, P., Su, Y., Guo, S., & Su, Z. (2021). Acousto-ultrasonics-based health monitoring for nano-engineered composites using a dispersive graphene-networked sensing system. Structural Health Monitoring, 20(1), 240–254. Copyright © The Author(s) 2020. DOI: 10.1177/1475921720929749.

# Acousto-ultrasonics-based Health Monitoring for Nano-engineered Composites Using a Dispersive Graphene-networked Sensing System

Yehai LI [a,b,c,‡], Kai WANG [c,‡], Qiang WANG [d], Jianwei YANG [c], Pengyu ZHOU [c], Yiyin SU [c], Shifeng GUO [a,b] and Zhongqing SU [c,e*]

[a]Guangdong Provincial Key Lab of Robotics and Intelligent System

Shenzhen Institutes of Advanced Technology, Chinese Academy of Sciences, Shenzhen, P.R. China

[b]CAS Key Laboratory of Human-Machine Intelligence-Synergy Systems

Shenzhen Institutes of Advanced Technology, Shenzhen, P.R. China

[c]Department of Mechanical Engineering

The Hong Kong Polytechnic University, Hung Hom, Kowloon, Hong Kong SAR

[d]College of Automation

Nanjing University of Posts and Telecommunications, Nanjing, P.R. China

[e]The Hong Kong Polytechnic University Shenzhen Research Institute,

Shenzhen 518057, P.R. China

**Submitted to *Structural Health Monitoring: An International Journal***

(submitted on 18th October 2019; revised and re-submitted on 25 March 2020)

‡ These authors contributed equally to this work.

* To whom correspondence should be addressed. Tel.: +852-2766-7818, Fax: +852-2365-4703; Email: Zhongqing.Su@polyu.edu.hk (Prof. Zhongqing SU, *Ph.D.*)

**Abstract**

Sensing is a fundamental yet crucial part of a functional structural health monitoring (SHM) system. Substantial research has been invested in developing new sensing techniques to enhance sensing efficiency and accuracy. Practical applications of SHM approaches to real engineering structures require strict criteria for the sensing system (*e.g.,* weight, position, intrusion and endurance), which challenge existing sensing techniques. The boom in nanotechnology has offered promising solutions for the development of new sensing approaches. However, a bottleneck still exists when considering the density of sensors and surface-mounted modality of installation. In this study, graphene nanoparticles are dispersed into a glass fibre/epoxy composite to form a dispersive network sensing system. The piezoresistivity of the graphene-formed network (GN) changes locally as a result of the change of inter-nanoparticle distances which triggers the "tunnelling effect" and drives the sensor to respond to propagating elastic waves. Due to the dense graphene network formed within the composite, only a small area is required, functioning as a single sensing element to capture ultrasonic waves. To validate such capability, passive acoustic emission (AE) tests and active guided ultrasonic wave (GUW) tests are performed individually. The graphene-networked sensing system can precisely capture wave signals which contain effective features to identify impact spot or damage location. Integrating passive GN and active lead zirconate titanate wafers (PZTs) can form a dense network, capable of fulfilling general SHM tasks.

***Keywords*:** nano-engineered composites; structural health monitoring; acoustic emission; guided ultrasonic waves; graphene-networked sensing system

## 1. Introduction

The concept of structural health monitoring (SHM) has been developed to address continuous (or real-time without downtime) in-situ (without disassembly required), condition-based and automated surveillance of the overall integrity of structures during their whole life cycle, thereby enhancing structural and system safety, driving down maintenance costs such as time and labour, and potentially extending the residual life of aging structures. A complete SHM system is established via combining a sensing system that is integrated as part of the structure itself, a pre-established theoretical model, advanced signal-processing, damage diagnosis algorithm, and data management system. The sensing system is fundamental and also crucial for achieving an effective SHM scheme.

Sensors and sensor networks, akin to the neural networks in biological systems, play the most pivotal role in acquiring environmental information and perceiving structural responses, on which basis the health status of a structure under inspection can be evaluated. Thus, the importance of selecting appropriate of sensor type and optimizing a configured sensor network cannot be overemphasized,[1-4] which require certain features to fulfil the various detection tasks in the SHM process: (a) verified acquisition of changes in the host structure, but invulnerability to noise from environmental change; (b) reliable transportation of captured signals; (c) minimal intrusion to host structures; (d) endurance for working conditions, considering harsh environments and loading; and (e) easy installation and operation. Furthermore, when applied to a real aerospace structure, to which the weight and volume penalty due to the introduction of a sensor network to the structure is a concern, sensors shall be of small size, light mass, reduced use of wires/cables, low cost, and minimal deterioration with aging.[4, 5] Diverse human-made sensing elements such as metal strain gauges, optical fibres[6, 7], electromagnetic acoustic transducers (EMAT)[8, 9], piezoceramic transducers[10], lead zirconate titanate (PZT) wafers[11] and nanomaterial sensors[12, 13] have been developed and deployed on engineering structures to form sensor networks. As external additions to the host structures, these sensors must be either surface-mounted or internally embedded in the inspected structures. Combinations of a certain number of such sensors can form a sensing network.

A dense sensor network is always preferred in the hope of acquiring rich information, but the integration of multiple of sensors unavoidably adds a burden to the host structure.[14] With the surface-mounted modality of installation, sensors together with unwieldy cables and wires in a dense network for linking individual sensors would impose extra load and weight/volume penalty on host structures. Some researchers have proposed the use of wireless technology in sensor networks to reduce connection problems significantly.[15, 16] However, a surface-mounted sensor network exposed to a cruel service environment is vulnerable to corrosion/deterioration, and runs a high risk of detaching from the host structure, owing to degradation of the adhesive layers between host structure and sensors. Embedding sensors and wires in composite structures and isolating sensors from external environments can effectively minimize measurement noise and mitigate ageing due to environmental effects.[17, 18] However, such manoeuvres can impair local material strength, introducing defects, stress concentration and debonding.[5] To minimize such risks in engineering practice, a limited number of sensors are placed at strategic sites to form a "sparse" sensor network, assisted by specific signal-processing algorithms to manipulate the "limited" information acquired. Compared to a dense network, a sparse sensor network is understandably incapable of providing high-precision monitoring, due to the reasons such as quick wave attenuation as a result of long wave propagation distance, restricted coverage for a structure with complex geometry and influence of structural boundaries, as well as limited information carried by each sensing path.[1, 2]

In today's high-frequency guided ultrasonic wave (GUW) -based SHM methods, PZT wafers and optical fibres are two major preferred sensor elements. Besides the inevitable intrusion to the host structure mentioned above, these sensors *per se* have other problems. Ultrasonic signals captured via mounted PZT wafers or optical fibres are prone to the viscoelastic behaviour and bonding quality of the adhesive layer.[19, 20] Embedded PZT wafers in composites can become short-circuited with conductive carbon fibres when the composites undergo high temperatures up to 180°C and pressures up to circa 700kPa in autoclaving process. Use of anti-temperature/pressure insulating films can circumvent this problem, but it may be at the cost of introducing incompatibility between the films and the epoxy matrix and accordingly affecting the interface strength.[21] Optical sensors such as fibre Bragg gratings (FBG sensors) may face problems such as infeasibility of repair or replacement, strong directivity, and relatively high cost.[22, 23]

With advances in electronics and manufacturing, miniaturization of these sensors could solve some of the described problems, but still encounters difficulty in striking a balance between "sensing cost" (*i.e.,* high price, weight penalty, intrusion) and "sensing effectiveness" (*i.e.,* sufficient information to detect damage).[24] Thanks to recent advances and breakthroughs in material chemistry, electronics and manufacture, researchers have tried to develop new ways to design and implement sensors and sensing systems. Nano-engineered composites with fully dispersive sensing networks provide a possible solution for composite structures to circumvent such problems. Loh *et al.*,[25] Naghashpour *et al.*,[26] and Tallman *et al.*,[27] each developed tomography algorithms based on electrical impedance or resistance change in nano-engineered composites. García *et al.*[28] investigated the frequency response and mode shapes of a nano-engineered composite beam under vibration via monitoring the overall resistance variation. However, such self-sensing approaches that rely on global and static/low-frequency methods usually feature low sensitivity and vulnerability to noise, and provide qualitative damage assessment only. Dense electrodes and messy associated circuits would be another obstacle to implementing them.

In this study, Lamb wave diagnosis technology is integrated with the self-sensing capability of a graphene-formed network (GN) dispersed in a composite material, presenting an innovative acousto-ultrasonics-based SHM strategy in nano-engineered composite structures. Due to their "dispersive" nature, such sensing systems are relatively impervious to environmental influences and have good endurance. Furthermore, thanks to the infinitesimal scale and high strength of nanoparticles, they would not cause notable intrusion to the host structure. Both passive and active SHM strategies are tested for evaluating feasibility. Certain algorithms are applied to extract source location information and to image evaluation results. Thus a non-intrusive, well-qualified sensing system is proposed for future SHM development.

## 2. Fabrication of Nano-engineered Composite Laminate

The graphene-enriched glass fibre/epoxy laminate was manufactured by hand lay-up followed by vacuum bagging, and reinforced by plain-woven glass fibre fabrics. Epoxy Araldite GY 251 and hardener Aradur HY 956 were used as the matrix material. 1.0 wt% graphene was dispersed into epoxy resin as the optimal quantity before application on fabrics.[29] The mixture was initially mechanically stirred while being heated to 80 °C and then treated in an ultrasonic bath to obtain a homogeneous mixture (**Figure 1**). Each glass fibre layer was impregnated with graphene-enriched epoxy using a hand roller (**Figure 2a**). Eight layers of (0, 90) plain woven fabrics were used to lay up a ~1.2 mm thick laminate plate with a quasi-isotropic configuration of $[(0, 90)/(+45, -45)/(+45, -45)/(0, 90)]_s$. The laminates were cured with the help of standard vacuum bagging procedure as illustrated in **Figure 2b**. Cured laminates were then trimmed around the edges to the final dimensions of 400 mm × 400 mm.

The dispersed graphene nanoparticles form a nanostructured network within the insulating polymer matrix. Quantum tunnelling effect allows transfer of electrons among indirectly contacted nanoparticles. Thus, the resistance of local network is comprised of the particle intrinsic resistance and tunnelling resistance, subjected to inter-particle distance.[30] Under an elastic wave-induced strain disturbance, local resistivity changes accordingly. Such behaviour is also referred to as piezoresistivity.

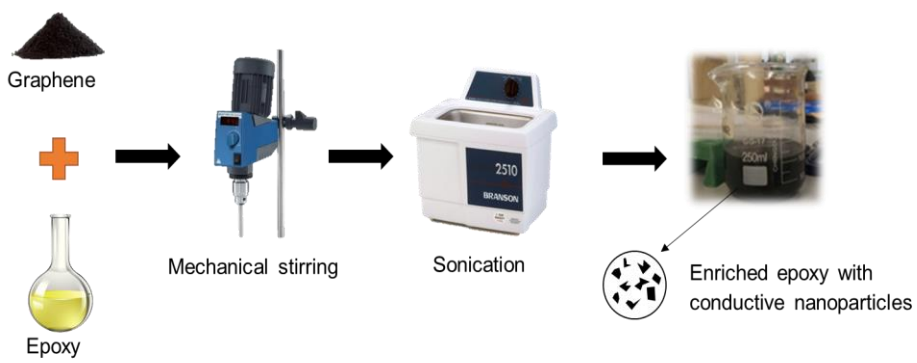


**Figure 1.** Schematic of the dispersion process of graphene-enriched epoxy resin.

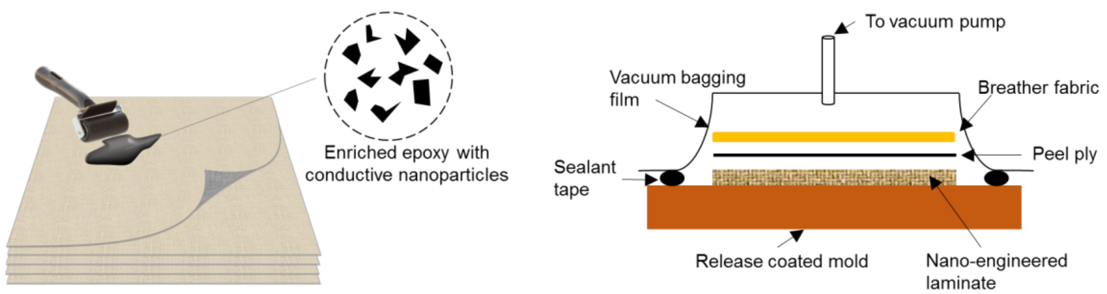


(a) (b)

**Figure 2.** Schematic of (a) hand lay-up and (b) vacuum bagging procedure used to manufacture the nano-engineered laminate.

## 3. Passive Impact Localization Using Acoustic Emission (AE)

### 3.1 Methodology

According to our previous study, a pair of electrodes on the surface of the composite plate thus made can extract the local response of Lamb waves propagating in the plate structure via the dispersive GN.[29] Instant impact will create an acoustic source which emits elastic waves along the structure. These AE signals carrying source information are captured by GN and recorded at different sensing locations. The most common algorithm to locate the AE source is the "time differences of arrival" (TDoA).[31] As illustrated in **Figure 3**, with the impact occurring at *(x, y)*, AE signals reach two sensing points at time $t_a$ and $t_b$,

$$\begin{aligned} t_a &= t_0 + \Delta t_a, \\ t_b &= t_0 + \Delta t_b \end{aligned} \quad \textbf{(1)}$$

where $t_0$ is the moment when the impact occurs. $\Delta t_a$ and $\Delta t_b$ are the subsequent travelling times of AE signals from the source to sensing points *a* and *b*. The TDoA obtained from arrived signals at *a* and *b* can be expressed as

$$\begin{aligned} \Delta t_{ab}(x,y) &= t_a - t_b = (t_0 + \Delta t_a) - (t_0 + \Delta t_b) \\ &= \frac{\sqrt{(x-x_a)^2 + (y-x_a)^2} - \sqrt{(x-x_b)^2 + (y-x_b)^2}}{v_{wave}}. \end{aligned} \quad \textbf{(2)}$$

With prior knowledge of wave speed $v_{wave}$ (derived from either dispersion curves or experiments) and coordinates of points *a* and *b*, the impact spot can be located as a hyperbolic curve (green dotted line in **Figure 3**). Usually, a multitude of sensing points used leads to fine resolution in the final results.

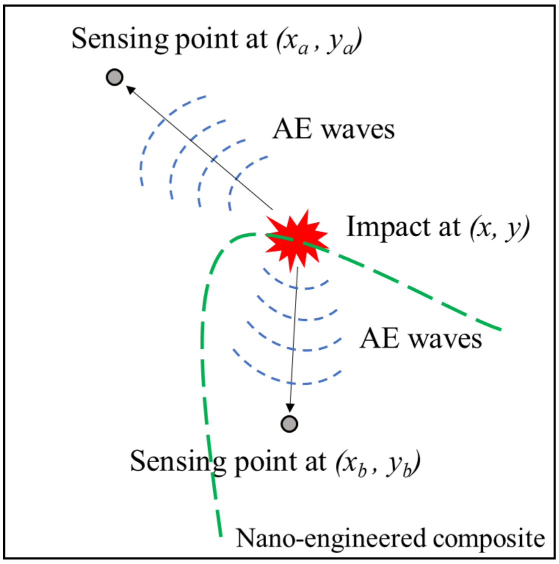


**Figure 3.** Illustration of TDoA algorithm.

The AE source localization procedure in this study includes several steps (**Figure 4**):

(i) When AE signals generated by an impact cross a pre-set threshold in one of the sensing points, the trigger information is sent to all remaining devices. At that moment, the captured signal from the first sensor is treated as the reference for the timeline of all obtained signals and further tomography.

(ii) In most cases, AE signals from the impact spot are broadband dispersive waves, which make it very difficult to extract useful features such as TDoA. Thus a narrowband filter (*e.g.,* wavelet transform (WT)) is required to identify individual wave components which can help determine the TDoA.

(iii) The TDoA can be acquired by comparing the leading edge against a pre-set threshold, energy peak, or cross-correlation of the signals captured at different spots.[32] Each pair of sensing points should image a hyperbolic curve as an estimation of the source location.

(iv) Tomography methods (*e.g., delay-and-sum*) are then used to superpose multiple images from all other sensing points pairing with the reference one.

(v) The final source location is represented by the pixel value of the image, which is the two-dimensional mesh of the inspected structure. Each image pixel represents the probability of occurrence of an impact event and is determined using a probability-based tomography algorithm.[31]

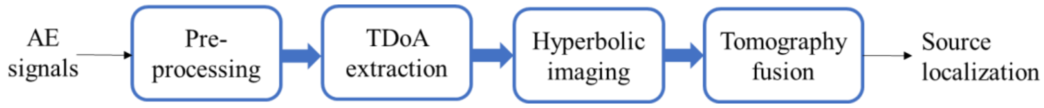


**Figure 4.** Typical steps for AE source localization procedure.

### 3.2 Experimental Set-up

Eight sensing points (Pi, i=1,2…8) evenly distributed on the surface, with the angular spacing of 45°, were used to form a passive sensing system for impact localization. Packaged electrodes and circuits were attached to each point using silver conductive adhesive (**Figure 5**). It is noteworthy that the adhesive was used only for creating electric connection and transmitting signals captured by dispersive GN in the structure. Thus the bonding quality and viscoelastic behaviour of the adhesive layer, from which a conventional surface-mounted PZT sensor usually suffers, shall cause ignorable disturbance to captured signals, provided good electric connection remains. AE signals from all points were received simultaneously by a self-assembled acousto-ultrasonics-based SHM nano-sensing system (**Figure 6a**). This system was specifically designed for a nanoparticle-formed network, consisting of a multi-channel data acquisition (DAQ) module (a self-designed signal amplifier and a digitizer), a GUW active module (a power amplifier and an arbitrary waveform generator (AWG)) and a central control module. The digitizer (NI® 5105, 60 MHz, 8-Channel, 12-Bit PXI Oscilloscope) and AWG (NI® PXI-5412) were integrated on a PXI bus platform (NI® PXIe-1071). This system was capable of wave sensing and actuating functions; this AE experiment, only the sensing function was activated. The AE source was created via dropping a steel ball (diameter 10 mm, weight 10 g) from a 300 mm height. The impact energy (~0.03 J) generated elastic waves which propagated omnidirectionally over the plate. Once the wave signals crossed the pre-set threshold, the whole system was triggered and recorded signals captured at each point. The central control module (**Figure 6b**) was developed on a NI LabVIEW platform for command control, digital signal-processing (*e.g.*, time-frequency analysis, Hilbert transform, bandpass filter) and further construction of diagnostic images.

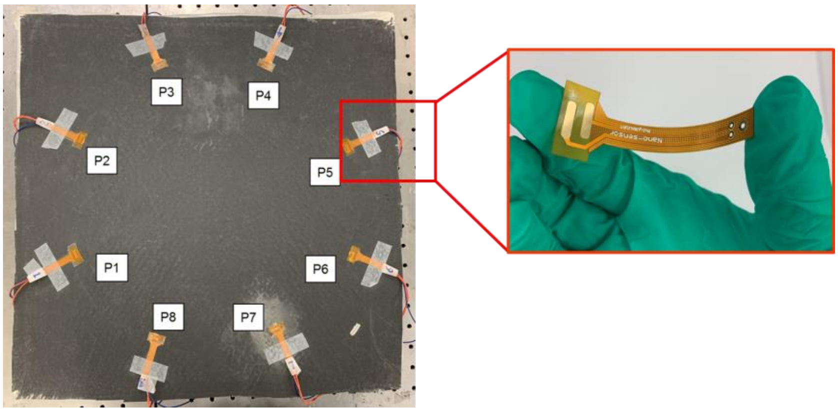


**Figure 5.** Passive sensing system set-up with packaged electrodes and circuits.

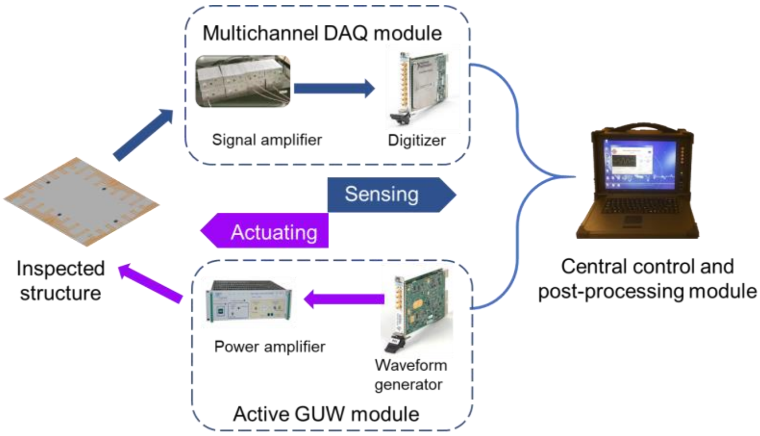


(a)

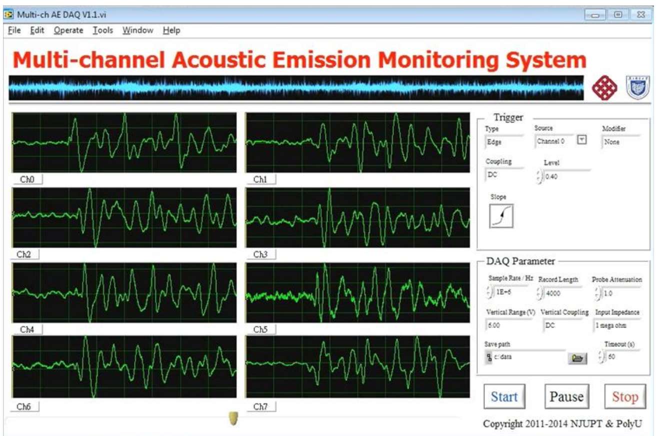


(b)

**Figure 6.** (a) Self-assembled acousto-ultrasonics-based SHM nano-sensing system; (b) self-developed multi-channel DAQ program interface.

### 3.3 Results

Without loss of generality, for analysis and validation purposes, representative signals captured at point 1 and point 6 are compared with nearby surface-mounted PZT sensors, under a same drop impact precisely located via a tube. The raw AE signals captured by GN and nearby PZT sensor are presented in Figure 7a, where the different initial moments are due to the different amplitudes of captured signals and the pre-set trigger thresholds. Figure 7b shows the corresponding spectra of two signals, obtained via Fast Fourier transform, revealing that the domain energy of the captured AE signals is confined in a frequency range below 10 kHz. Therefore, a lowpass filter with a cut-off frequency of 10 kHz is employed to eliminate noise. However, the signals obtained are still quite broadband, making it difficult to extract precise time features. Thus the signals require further processing to select wave components at a certain frequency. A WT is commonly used to analyse dispersive wave signals, the most popular families being Haar, Daubechies, Symlet, Coiflets, Biorthogonal, Meyer, and Morlet transforms. In this study, the Daubechies wave family (dbN) is employed to decompose the captured AE signals, which presents sufficient time-frequency localization for resolving abrupt changes.[4] **Figure 8** shows the obtained frequency-time spectra of AE signals captured at two sensing locations. It is easy to observe the movement of the first arriving wave packets in time domain relatively to different sensing locations, which represents the TDoA of first-triggered and later-response wave signals. It is worth noticing that the AE signals obtained by GN and PZT are not identical in either the time or the frequency domain. The differences can be attributed to the distinct sensing mechanisms between two kinds of sensors in responding guided waves. A surface-mounted PZT sensor captures guided waves via the piezoelectric response to surface dynamic strain transferred through the bonding layer,[33] while the dispersive GN perceives wave-induced strain within the structure via the piezoresistivity based on the tunnelling effect.[34] Nevertheless, the WT results demonstrate that the time features of different frequencies share similar delay patterns between the first-triggered and later-response signals, which validates the feasibility of achieving AE source localization using GN.

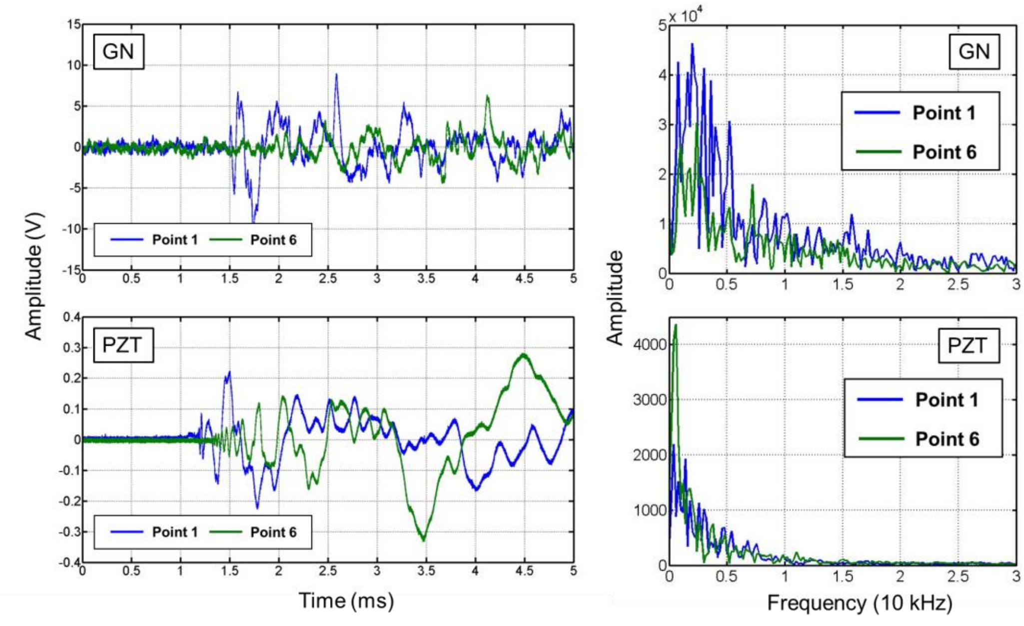


**Figure 7.** (a) Raw AE signals and (b) corresponding frequency spectra of GN and nearby PZT sensor, respectively.

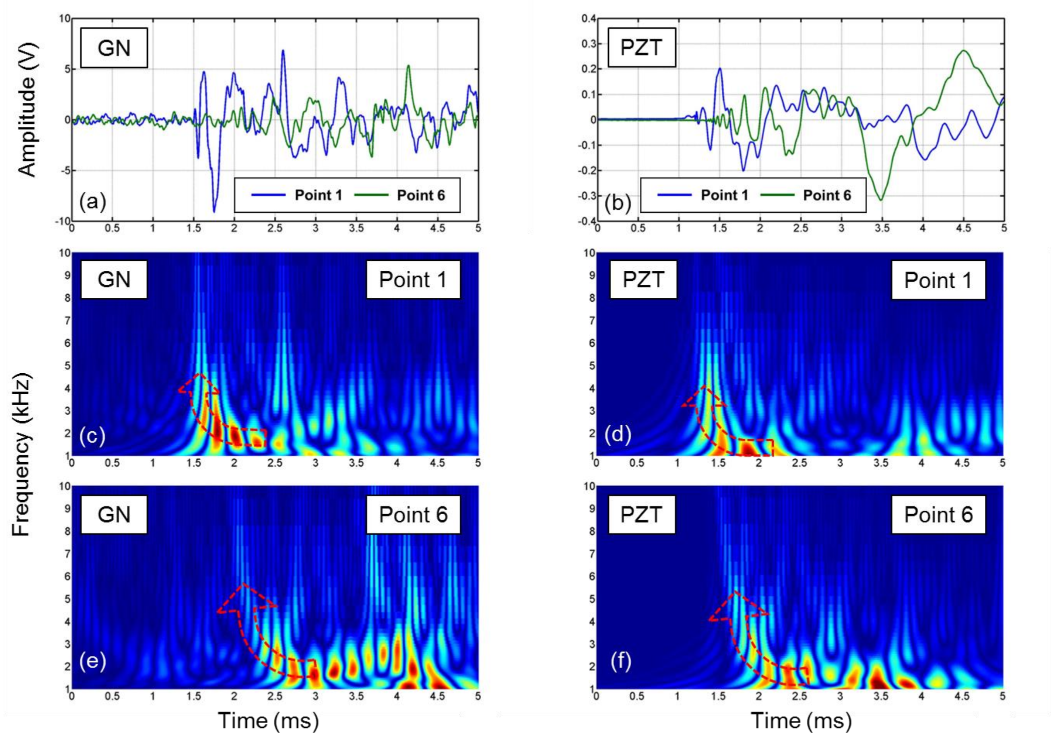


**Figure 8.** De-noised signals (a & b), frequency-time spectra via WT of first-triggered point 1 signal (c & d) and later-response point 6 signal (e & f) of GN and PZT sensor, respectively.

To better understand the components of arrived waves, the dispersion curves of such a composite plate are calculated via the software DISPERSE in **Figure 9**.[35] The frequency band of acquired AE signals (as highlighted with a dotted rectangle) is significantly lower than the cut-off frequencies of those high-order wave modes (such as the first- and second-order, symmetrical and antisymmetric modes, denoted as $S_1$, $S_2$, $A_1$ and $A_2$, respectively, in **Figure 9**). Thus only the two fundamental Lamb waves, the zeroth-order symmetrical mode (also known as the extensional mode, denoted as $S_0$ hereinafter) and the zeroth-order antisymmetric mode (also known as the flexural mode, denoted as $A_0$ hereinafter), propagate through the plate. Such a frequency band is also within the non-dispersive region of $S_0$ mode; in contrast, $A_0$ wave mode presents phenomenal dispersive behaviour in this frequency range. For out-of-plane excitation, generally the energy in the $A_0$ mode is considerably greater than that rendered by the $S_0$ mode. This outcome can be validated by comparing the energy tips of the first arriving wave packets at different frequency components from the spectra in **Figure 8** (red dashed arrows), which follows well the dispersion pattern of the $A_0$ mode, *i.e.*, the wave velocities increase with an increase in frequency in the low-frequency range. On the other hand, no significant sign of $S_0$ waves can be observed, which should arrive earlier than $A_0$ waves.

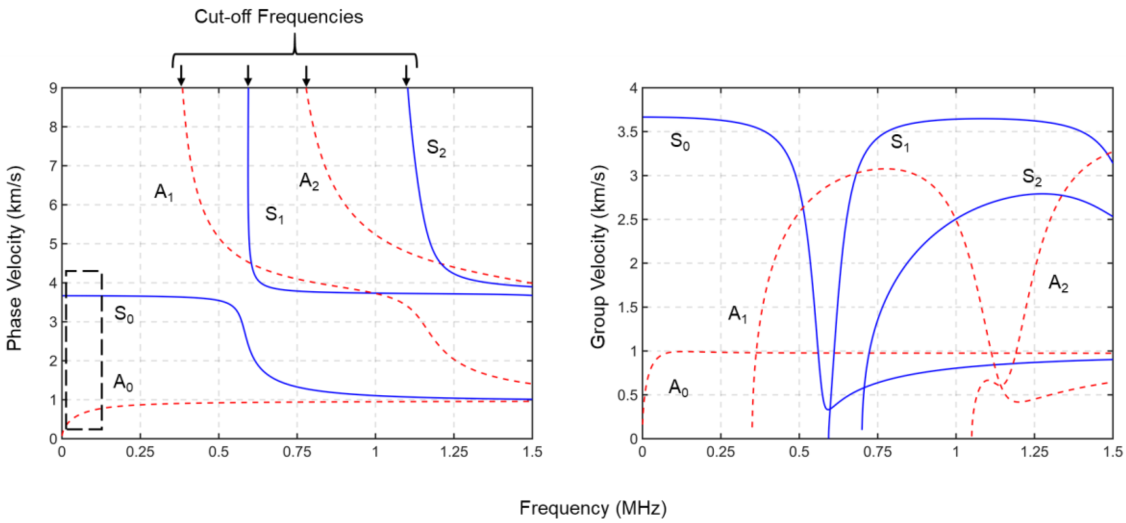


**Figure 9.** Dispersion curves of the manufactured composite plate.

The wave component of 6 kHz is then chosen for further processing, due to relatively stable wave velocity and narrow wave dispersion. Its associated group velocity can be derived via the signals from PZT sensors. The Hilbert transform is used to obtain the energy envelope curves of the first arriving wave packets, whereas other wave packets are flatted as undesirable information. A probability-based diagnostic imaging (PDI) tomography is used to visualize the source location with the *delay-and-sum* algorithm. Using PDI, the inspection region of the composite structure is meshed virtually, and projected to an image with each image pixel corresponding exclusively to a spatial point in the inspected region. The pixel value for a pair of AE signals captured in two sensing locations can be defined as

$$I_{ab}\left(x,y\right)=\max(\mathrm{E}_a+\mathrm{E}_b(\Delta_{ab}\left(x,y\right))), \quad \textbf{(3)}$$

where E is the energy packet of signals after processing. The time delay $\Delta_{ab}(x, y)$ is the TDOA of the sensing points *a* and *b* for each spot within the inspected area, which can be obtained from **Equation (2)**. The signals at points *a* and *b* are delayed and summed accordingly and the maximum value of the summation results can be linked to the probability of occurrence of an impact spot.[36] In accordance with **Equation (2)** and **(3)**, locations featuring the same TDoA in the image will have the same pixel value as a hyperbola curve with point *a* and point *b* being the two foci. In this example, the pair of sensing points 1 and 6 yields a tomography image as in **Figure 10**. The true drop impact spot is also identified, which is exactly located within the "red zone" (the area with the highest probability of source spot). With point 1 as the reference for all other points, a total of seven pairs of AE signals can be obtained via similar signal-processing steps. The final tomography is obtained by superposing all PDI results, with examples in Figure 11a. Figure 11b shows the combined results of four different impact tests, all of which have proven good precision of the approach in identifying the acoustic source (i.e., damage) using AE signals. Thus, the sensing system formed by GN is capable of capturing AE signals in which source-related information help locate the impact spot.

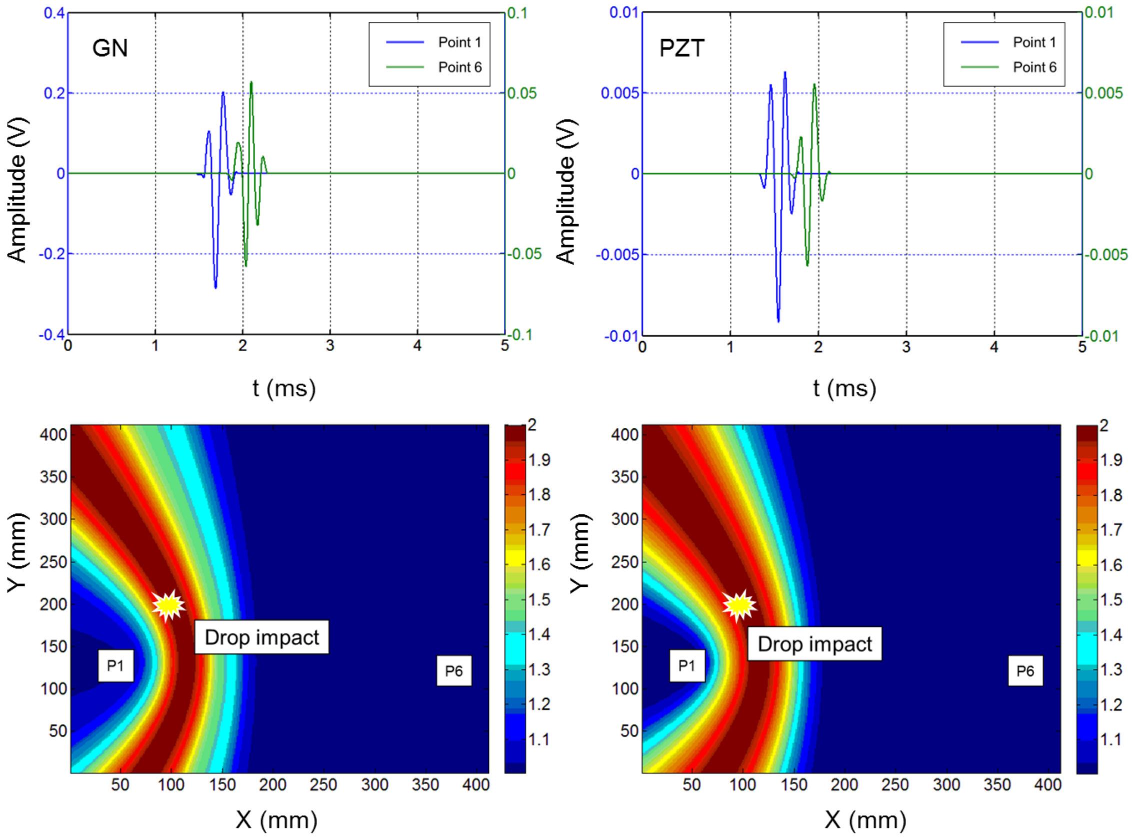


**Figure 10.** First arriving wave packets at 6 kHz of GN and PZT and their corresponding *delay-and-sum* image.

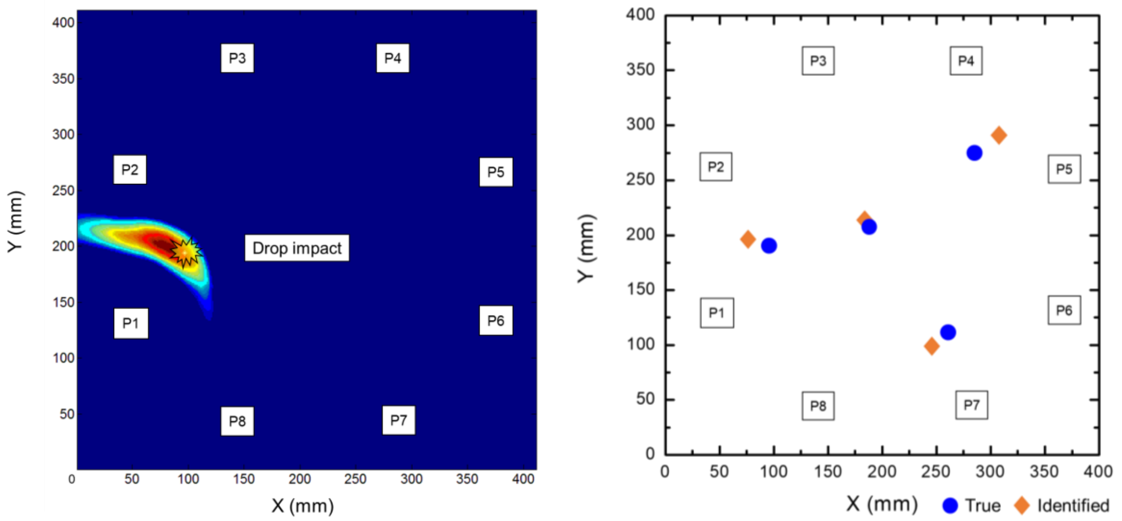


(a) (b)

**Figure 11.** (a) Representative tomography of impact AE source localization (b) combined results of four impact tests.

## 4. Active Damage Identification Using Guided Ultrasonic Waves (GUWs)

### 4.1 Methodology

In active damage detection technology, GUWs are excited via certain actuators. When these GUWs propagate along an inspected structure, damage such as voids, delamination, and mass change leave their "fingerprints" in the received waves captured at sensing points, either in a linear domain (*e.g.* damage-scattered waves, energy dissipation, phase conversion), and/or a nonlinear domain (*e.g.* high-order harmonics, modulation spectroscopy).[37] Our GN is ready to capture these features for damage assessment. Then, a location algorithm is applied to deal with damage-related features and then identify the damage. The time-of-arrival (ToA) algorithm is a common method used for the damage-scattered waves features. As illustrated in **Figure 12**, the location of damage can be triangulated by

$$t_{A-D-S} - t_{A-S} = \left( \frac{L_{A-D}}{v_1} + \frac{L_{D-S}}{v_2} \right) - \frac{L_{A-S}}{v_1} = \Delta t \,, \tag{4}$$

in which

$$\begin{aligned} L_{A-D} &= \sqrt{\left(x_D - x_A\right)^2 + \left(y_D - y_A\right)^2} \\ L_{D-S} &= \sqrt{\left(x_S - x_D\right)^2 + \left(y_S - y_D\right)^2} \;, \\ L_{A-S} &= \sqrt{\left(x_S - x_A\right)^2 + \left(y_S - y_A\right)^2} \end{aligned}$$

where $t_{A\text{-}D\text{-}S}$ and $t_{A\text{-}S}$ are the ToA of the waves propagating from the actuator to the damage and then to the sensing point and ToA of the incident waves propagating directly from the actuator to the sensing point, respectively. $v_1$ denotes the group velocity of the incident wave from the actuator and $v_2$ is the group velocity of the damage-scattered waves. $L_{A\text{-}D}$, $L_{D\text{-}S}$ and $L_{A\text{-}S}$ represent the distance between the actuator ($x_A$, $y_A$) and the damage ($x_D$, $y_D$), the distance between the damage centre ($x_D$, $y_D$) and the sensing point ($x_S$, $y_S$) and the distance between the actuator ($x_A$, $y_A$) and the sensing point ($x_S$, $y_S$), respectively. The positions of the actuator

($x_A$, $y_A$) and the sensing point ($x_S$, $y_S$) are already known via either theoretical analysis or experiments, and $\Delta t$ is to be determined from captured GUW signals. With known $v_1$ and $v_2$, the solution to **Equation (4)** is an elliptical or an ellipse-like locus with the actuator and the sensing point being the foci, as shown by the green dotted line in **Figure 12**. Since the GN is dispersed all over the fabricated composite structure, GUW acquisition can be achieved at any site of the composite. With a sufficient number of sensing paths, the location of the damage in the composite structure can be precisely solved by mathematically seeking the intersection of all loci.

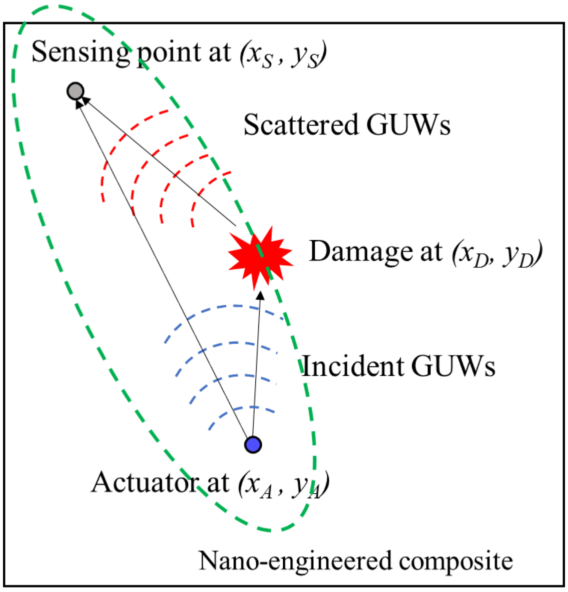


**Figure 12.** Illustration of ToA algorithm.

## 4.2 Experimental Set-up

Four packaged PZT wafers (Wi, i=1,2,3,4) were bonded on the surface of the inspected plate as shown in **Figure 13(a)**. Each wafer acted as the actuator in sensing paths with its opposite sensing points of GN (Pi, i=1,2,3…8). Such a mixed PZT-GN sensing system, consisting of active PZTs and passive GN, can form a sufficiently dense network (24 sensing paths), as illustrated in **Figure 13(b).** The actuating function of our SHM nano-sensing system (as shown in **Figure 6a**) was used to stimulate GUWs via PZT wafers. As GUWs propagate along the structure, they were captured by certain sensing points of the passive GN. Then the sensing function was utilised and transferred data into the control module. In such intact condition, each of the actuators (Wi, i=1,2,3,4) was excited in turn by 5-cycle *Hanning*-function-modulated sinusoidal tonebursts via the high-voltage amplifier (Ciprian® US-TXP-3)). All signals captured by sensing points were collected as the baseline signals. After that, a steel cylinder (diameter 20 mm, mass 200 g, as shown in **Figure 17**) was employed in this experiment as artificial damage, attached to the surface of the structure with glycerol as the couplant. Excitation was performed once again to obtain the current signals. 180 kHz and $S_0$ wave mode were selected for diagnostic wave signals, based on the previous frequency sweep test.[29] **Figure 14a** shows the amplitudes of captured wave signals at multiple frequencies, in which the peak value appears at around 180 kHz for the $S_0$ mode, similar to the trend of the signals captured by a PZT sensor. Such a phenomenon – the frequency-dependent signal amplitude, is mainly caused by *wave mode tunning* of PZT actuators.[38] This is because the tunnelling effect - sensing mechanism of GN, occurs in nanoscale, which provides a broadband frequency response[39] and thus the compensation for the frequency response from a PZT actuator is not of necessity. The wave speed of $S_0$ mode at 180 kHz was also calculated and verified by PZT sensors (~3311m/s, as shown in **Figure 14b**).

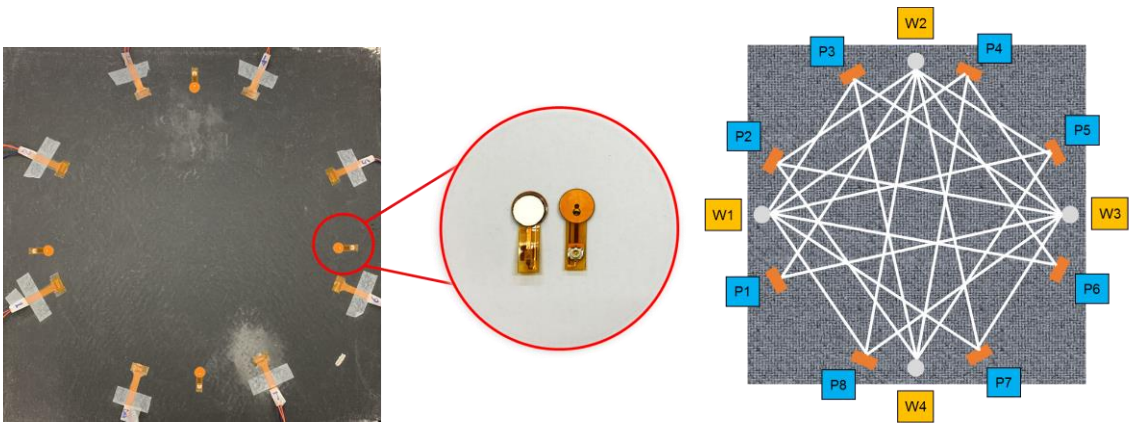


(a) (b)

**Figure 13.** (a) Mixed PZT-GN active sensing system and (b) formed sensing paths.

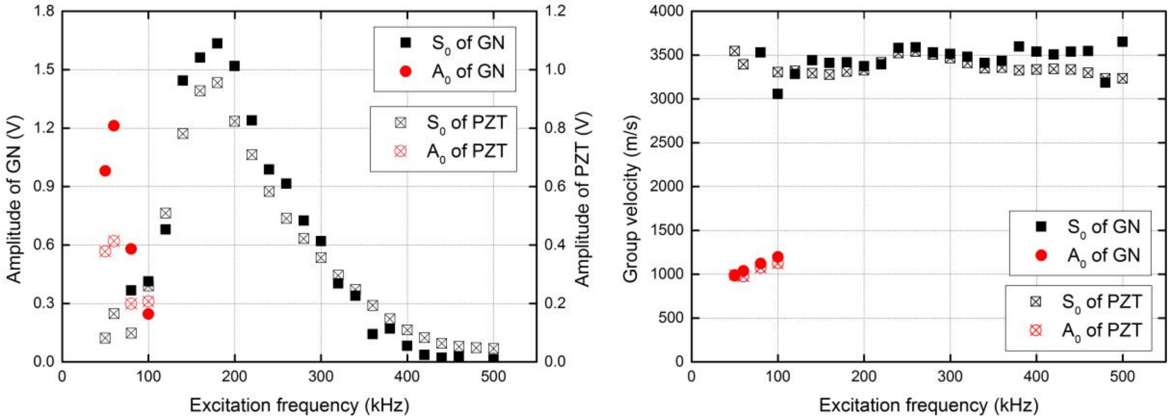


(a) (b)

**Figure 14.** (a) Comparison of amplitudes of response signals and (b) calculated group velocities by GN and PZT with different excitation frequencies.

### 4.3 Results

Without loss of generality, the signals of sensing path W1-P8 are exhibited for further signal-processing as an example (**Figure 15**). The crosstalk at the initial time (excitation moment) is attributed to spatial electromagnetic interference (EMI)[40] from the high-voltage amplifier. As it is known that this EMI crosstalk occurs only at the onset of excitation, it does not influence the identification of the subsequent GUWs. The first arriving wave packet appears to be the $S_0$ wave, based on the wave velocity. The damage-related features are hidden in the differential between the baseline and current GUW signals. To extract those features, the energy envelopes of both signals are compared and intersected to obtain the difference. As shown in **Figure 16**, the Hilbert transform is used to draw the profile of energy amplitude of baseline, current and differential signals. This permits easy identification of the coincidence of crosstalk and the first arriving incident $S_0$ waves. Furthermore, the damage-related feature is also easily observed as the peak in the signal differential.

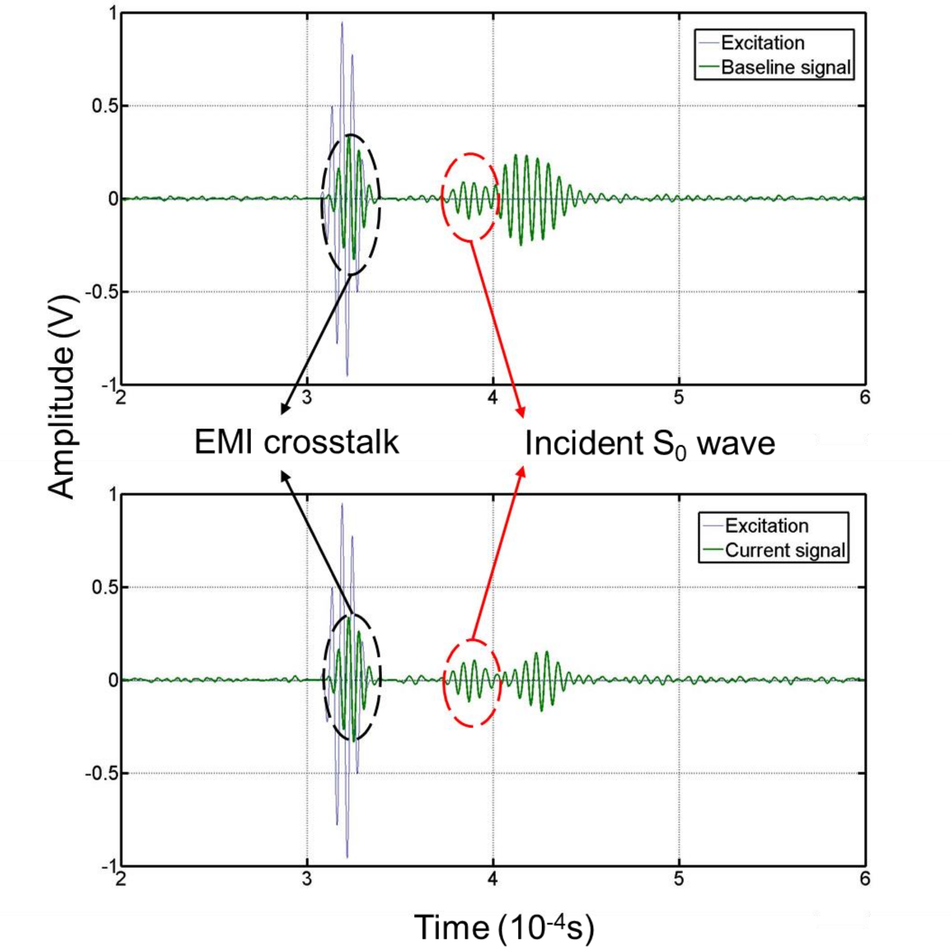


**Figure 15.** Baseline and current signals of sensing path W1-P8.

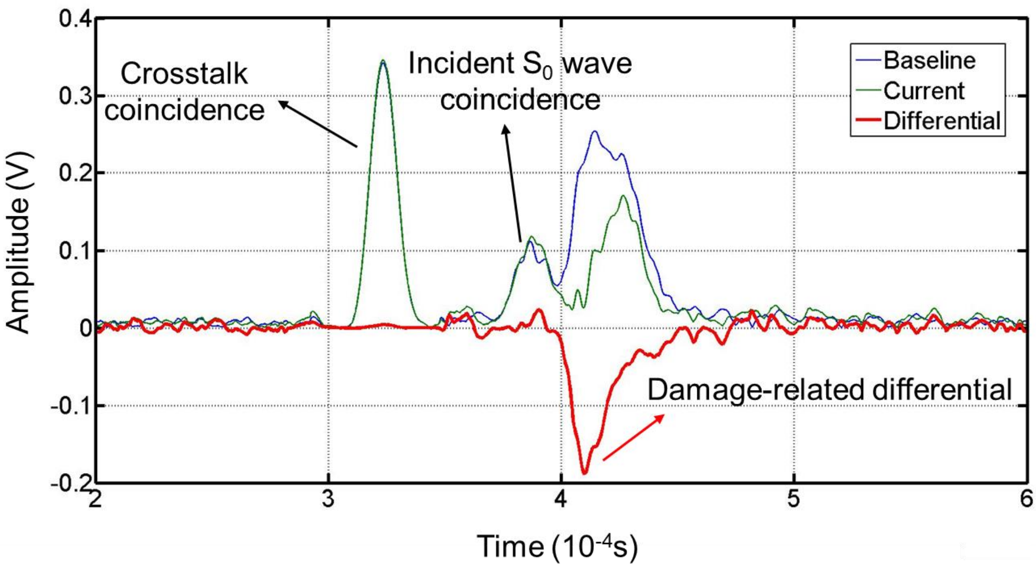


**Figure 16.** Energy envelopes of baseline, current signals, and their differential.

To facilitate visualization of the damage location, a PDI algorithm[41-43] is introduced which presents the diagnostic results in terms of probability in a two-dimensional greyscale image. The probability of the presence of damage at each spatial point is then calibrated in terms of the value of its corresponding pixel in the image, via

$$I(\mathrm{x}, y) = \sum_{r=1}^{n} W_r D_r \left( \frac{\sqrt{(x - x_A^r)^2 + (y - y_A^r)^2} + \sqrt{(x - x_S^r)^2 + (y - y_S^r)^2}}{v} \right), \tag{5}$$

where $I(x, y)$ denotes the field value at location ($x$, $y$) for the $r^{th}$ sensing path in the sensing network, which is linked to the probability of damage occurrence therein. $D_r(t)$ signifies the profile of energy amplitude of the relative difference between the baseline and current signals of the $r^{th}$ path, which can be obtained via the Hilbert transform:

$$D(\mathrm{t}) = H(f(\mathrm{t})) - H(f(\mathrm{t}_0)), \tag{6}$$

where $f$(t) and $f_0$(t) are the current and baseline signals, respectively. $W_r$ represents a weight coefficient to normalize the field value of the $r^{th}$ path as[44]

$$W_r = 1/\max D_r . \tag{7}$$

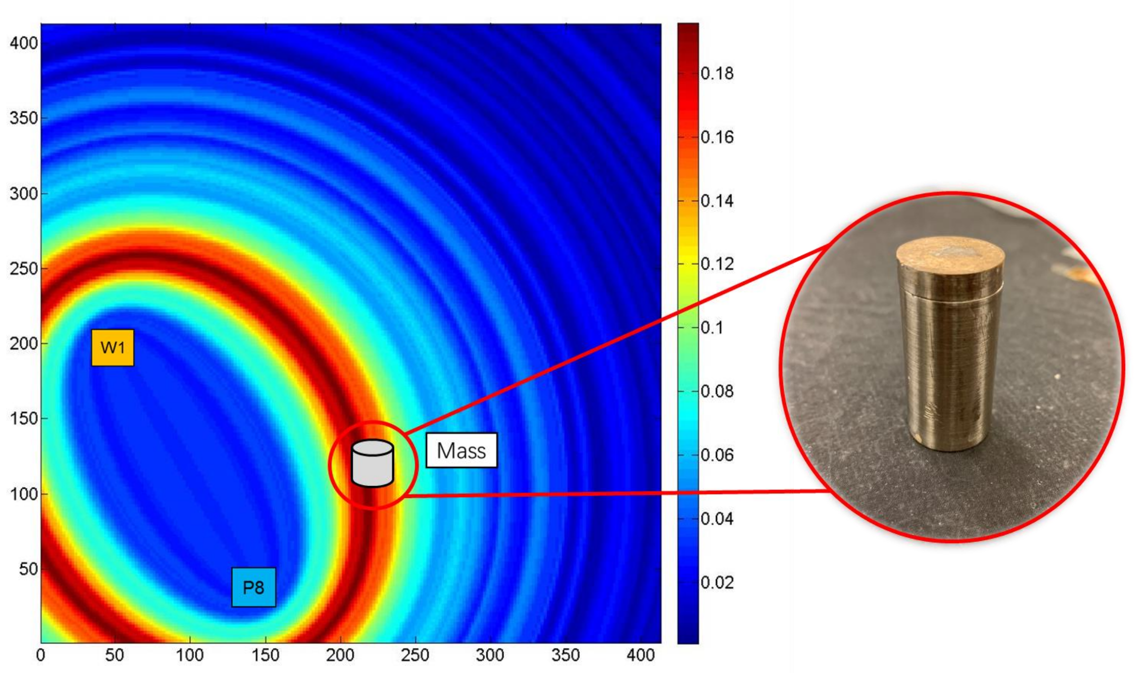


**Figure 17.** PDI result of W1-P8 sensing path with artificial damage.

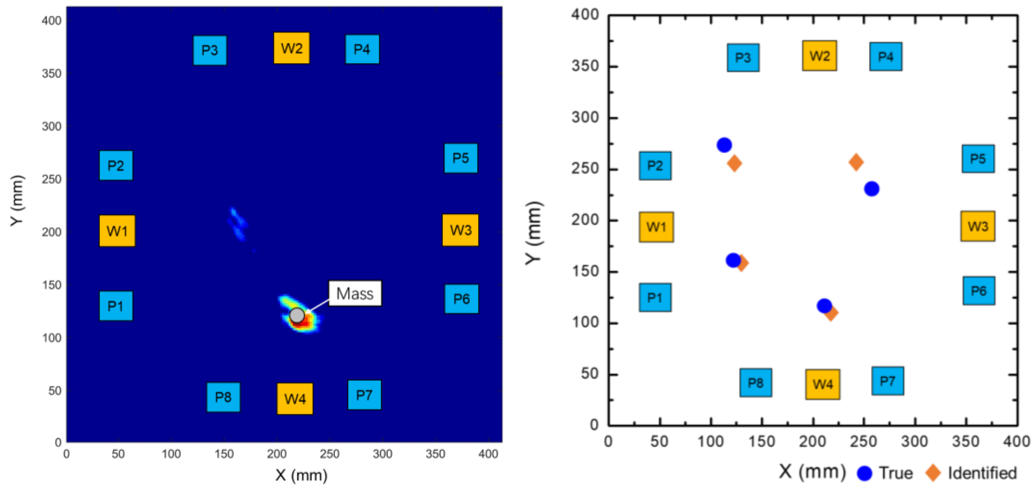


(a) (b)

**Figure 18.** (a) Representative PDI result of superimposing all sensing paths with artificial damage and (b) combined results of four artificial damage tests.

The PDI result of sensing path W1-P8 is illustrated in **Figure 17**, in which the highest pixel value loci in ellipse form cover the location of artificial damage. The final result is the superimposition of PDI results from all sensing paths, as shown in **Figure 18a**. A proper image threshold was used here to avoid the influence of structural boundary reflection and noise in the captured signals. This threshold was generally determined empirically and in this case, it was set to 30% of the maximum value. **Figure 18b** presents the combined results of four tests with different artificial damage locations, and good evaluation of the damage is achieved via the mixed PZT-GN sensing system.

## 5. Concluding Remarks

This study evaluates the possibility of using a GN sensing system in SHM technology, especially employing wave-based algorithms. The GN, as the passive sensing system, was used successfully to locate the impact spot via AE signals. When combined with a few PZTs, the mixed active sensing system provided a sufficiently dense sensing network to precisely identify the damage using GUWs-based technology.

During the experiments, the GN have exhibited certain features that qualify as a sensing system: (a) acquisition of wave signals is verified by comparison with conventional piezoelectric sensors; (b) as isolated from the environment, the graphene-networked sensing system in the structure will not be affected by the environmental corrosion or ageing deterioration. Technically speaking, the sensing capability continues to exist until failure of the host structure; (c) detachment issues and the viscoelastic behaviour of the adhesive layer in conventional surface-mounted sensor elements are eliminated, although the associated circuits still exhibit such issues; (d) GN causes only minimal burden or intrusion to the host structure. Graphene nanoparticles have been proved capable of functioning as reinforcement rather than defects in the epoxy-based materials, to enhance fracture toughness and elongate fatigue life.[45, 46] The host material can benefit from the high modulus and strength of nanoparticles. For as-produced laminates in this study, the elastic tensile modulus and ultimate tensile strength have been improved by 35% and 8%, respectively.[29]

In conclusion, these appealing features have blazed a new trail in developing dispersive sensing systems for SHM. The sensors can flexibly adapt to a curved surface, introduce ignorable weight/volume penalty to host materials, and be networked in a dense modality to provide rich information of the structural health status. It has proven accuracy and precision in responding broadband acousto-ultrasonic signals, with good compatibility with various passive and active SHM methods. Attempts of more different sensing network arrangements and damage detection methods will be explored in the future work.

**Acknowledgments**

This project was funded by the National Natural Science Foundation of China (Nos. 51875492 and 51635008) and the Hong Kong Research Grants Council via General

Research Fund (Nos. 15204419 and 15212417).

**References**


1. Su Z and Ye L. *Identification of damage using Lamb waves: from fundamentals to applications*. Springer Science & Business Media, 2009.
2. Diamanti K, Soutis C and Hodgkinson JM. Piezoelectric transducer arrangement for the inspection of large composite structures. *Composites Part A: Applied Science and Manufacturing* 2007; 38: 1121-1130. DOI: https://doi.org/10.1016/j.compositesa.2006.06.011.
3. Azarbayejani M, El-Osery AI, Choi KK, et al. A probabilistic approach for optimal sensor allocation in structural health monitoring. *Smart Mater Struct* 2008; 17: 055019. DOI: 10.1088/0964-1726/17/5/055019.
4. Staszewski W, Boller C and Tomlinson GR. *Health monitoring of aerospace structures: smart sensor technologies and signal processing*. John Wiley & Sons, 2004.
5. Paget C. *Active health monitoring of aerospace composite structures by embedded piezoceramic transducers*. Institutionen för flygteknik, 2001.
6. Wu Z, Qing XP and Chang F-K. Damage Detection for Composite Laminate Plates with A Distributed Hybrid PZT/FBG Sensor Network. *J Intell Mater Syst Struct* 2009; 20: 1069-1077. DOI: 10.1177/1045389x08101632.
7. Takagaki K, Minakuchi S and Takeda N. Process-induced strain and distortion in curved composites. Part I: Development of fiber-optic strain monitoring technique and analytical methods. *Composites Part A: Applied Science and Manufacturing* 2017; 103: 236-251. DOI: https://doi.org/10.1016/j.compositesa.2017.09.020.
8. Khalili P and Cawley P. Relative Ability of Wedge-Coupled Piezoelectric and Meander Coil EMAT Probes to Generate Single-Mode Lamb Waves. *IEEE Trans Ultrason Ferroelectr Freq Control* 2018; 65: 648-656. DOI: 10.1109/TUFFC.2018.2800296.
9. Ratnam D, Balasubramaniam K and Maxfield BW. Generation and detection of higher-order mode clusters of guided waves (HOMC-GW) using meander-coil EMATs. *IEEE Trans Ultrason Ferroelectr Freq Control* 2012; 59: 727-737. DOI: 10.1109/TUFFC.2012.2250.
10. Rao J, Saini A, Yang J, et al. Ultrasonic imaging of irregularly shaped notches based on elastic reverse time migration. *Ndt&e Int* 2019; 107: 102135. DOI: https://doi.org/10.1016/j.ndteint.2019.102135.
11. Yu X, Fan Z, Puliyakote S, et al. Remote monitoring of bond line defects between a composite panel and a stiffener using distributed piezoelectric sensors. *Smart Mater*

*Struct* 2018; 27: 035014. DOI: 10.1088/1361-665x/aaa69b.

12. Liao Y, Zhou P, Pan D, et al. An ultra-thin printable nanocomposite sensor network for structural health monitoring. *Struct Health Monit* 2019: 1475921719859338. DOI: 10.1177/1475921719859338.
13. Zhou P, Liao Y, Li Y, et al. An inkjet-printed, flexible, ultra-broadband nanocomposite film sensor for in-situ acquisition of high-frequency dynamic strains. *Composites Part A: Applied Science and Manufacturing* 2019; 125: 105554. DOI: https://doi.org/10.1016/j.compositesa.2019.105554.
14. Qiu L, Liu B, Yuan S, et al. Impact imaging of aircraft composite structure based on a model-independent spatial-wavenumber filter. *Ultrasonics* 2016; 64: 10-24. DOI: https://doi.org/10.1016/j.ultras.2015.07.006.
15. Yuan S, Lai X, Zhao X, et al. Distributed structural health monitoring system based on smart wireless sensor and multi-agent technology. *Smart Mater Struct* 2005; 15: 1-8. DOI: 10.1088/0964-1726/15/1/029.
16. Lynch JP and Loh KJ. A summary review of wireless sensors and sensor networks for structural health monitoring. *Shock and Vibration Digest* 2006; 38: 91-130.
17. Kudela P, Ostachowicz W and Żak A. Damage detection in composite plates with embedded PZT transducers. *Mech Syst Signal Pr* 2008; 22: 1327-1335. DOI: https://doi.org/10.1016/j.ymssp.2007.07.008.
18. Tang H-Y, Winkelmann C, Lestari W, et al. Composite Structural Health Monitoring Through Use of Embedded PZT Sensors. *J Intell Mater Syst Struct* 2011; 22: 739-755. DOI: 10.1177/1045389x11406303.
19. Park G, Farrar CR, Scalea FLd, et al. Performance assessment and validation of piezoelectric active-sensors in structural health monitoring. *Smart Mater Struct* 2006; 15: 1673-1683. DOI: 10.1088/0964-1726/15/6/020.
20. Han L, Wang XD and Sun Y. The effect of bonding layer properties on the dynamic behaviour of surface-bonded piezoelectric sensors. *Int J Solids Struct* 2008; 45: 5599-5612. DOI: https://doi.org/10.1016/j.ijsolstr.2008.06.003.
21. Paget C, Levin K and Delebarre C. *Behavior of an embedded piezoceramic transducer for Lamb wave generation in mechanical loading*. SPIE, 2000.
22. Campanella CE, Cuccovillo A, Campanella C, et al. Fibre Bragg Grating Based Strain Sensors: Review of Technology and Applications. *Sensors* 2018; 18: 3115.
23. Takeda N, Okabe Y and Mizutani T. Damage detection in composites using optical fibre sensors. *Proc Inst Mech Eng Part G J Aerosp Eng* 2007; 221: 497-508. DOI:

10.1243/09544100jaero148.
24. Ostachowicz W and Güemes A. *New Trends in Structural Health Monitoring*. Springer Vienna, 2016.
25. Loh KJ, Hou T-C, Lynch JP, et al. Carbon Nanotube Sensing Skins for Spatial Strain and Impact Damage Identification. *Journal of Nondestructive Evaluation* 2009; 28: 9-25. DOI: 10.1007/s10921-009-0043-y.
26. Naghashpour A and Van Hoa S. A technique for real-time detecting, locating, and quantifying damage in large polymer composite structures made of carbon fibers and carbon nanotube networks. *Struct Health Monit* 2015; 14: 35-45.
27. Tallman TN and Wang KW. Damage and strain identification in multifunctional materials via electrical impedance tomography with constrained sine wave solutions. *Struct Health Monit* 2016; 15: 235-244. DOI: 10.1177/1475921716635574.
28. García D, Trendafilova I and Inman DJ. A study on the vibration-based self-monitoring capabilities of nano-enriched composite laminated beams. *Smart Mater Struct* 2016; 25: 045011.
29. Li Y, Wang K and Su Z. Dispersed Sensing Networks in Nano-Engineered Polymer Composites: From Static Strain Measurement to Ultrasonic Wave Acquisition. *Sensors* 2018; 18: 1398.
30. Zeng Z, Liu M, Xu H, et al. Ultra-broadband frequency responsive sensor based on lightweight and flexible carbon nanostructured polymeric nanocomposites. *Carbon* 2017; 121: 490-501. DOI: 10.1016/j.carbon.2017.06.011.
31. Kundu T. Acoustic source localization. *Ultrasonics* 2014; 54: 25-38. DOI: https://doi.org/10.1016/j.ultras.2013.06.009.
32. Xu B, Yu L and Giurgiutiu V. Advanced methods for time-of-flight estimation with application to Lamb wave structural health monitoring. In: *Proceedings of the 7th International Workshop on Structural Health Monitoring, Stanford University, Palo Alto, CA* 2009.
33. Giurgiutiu V. Chapter 8 - Coupling of PWAS Transducers to the Monitored Structure. In: Giurgiutiu V (ed) *Structural Health Monitoring with Piezoelectric Wafer Active Sensors (Second Edition)*. Oxford: Academic Press, 2014, pp.395-443.
34. Li Y, Liao Y and Su Z. Graphene-functionalized polymer composites for self-sensing of ultrasonic waves: An initiative towards "sensor-free" structural health monitoring. *Compos Sci Technol* 2018; 168: 203-213. DOI: 10.1016/j.compscitech.2018.09.021.
35. Pavlakovic B and Lowe M. Disperse Software, v. 2.0. 16. *Mechanical Engineering,*

*Imperial College, London* 2005.

36. Qiu L, Liu M, Qing X, et al. A quantitative multidamage monitoring method for large-scale complex composite. *Struct Health Monit* 2013; 12: 183-196. DOI: 10.1177/1475921713479643.
37. Guan R, Lu Y, Wang K, et al. Fatigue crack detection in pipes with multiple mode nonlinear guided waves. *Struct Health Monit* 2019; 18: 180-192. DOI: 10.1177/1475921718791134.
38. Giurgiutiu V. Chapter 11 - Wave Tuning with Piezoelectric Wafer Active Sensors. In: Giurgiutiu V (ed) *Structural Health Monitoring with Piezoelectric Wafer Active Sensors (Second Edition)*. Oxford: Academic Press, 2014, pp.573-637.
39. Xu H, Zeng Z, Wu Z, et al. Broadband dynamic responses of flexible carbon black/poly (vinylidene fluoride) nanocomposites: A sensitivity study. *Compos Sci Technol* 2017; 149: 246-253. DOI: 10.1016/j.compscitech.2017.06.010.
40. Qiu L, Yuan S, Zhang X, et al. A time reversal focusing based impact imaging method and its evaluation on complex composite structures. *Smart Mater Struct* 2011; 20: 105014. DOI: 10.1088/0964-1726/20/10/105014.
41. Wang Q, Hong M and Su Z. An In-Situ Structural Health Diagnosis Technique and Its Realization via a Modularized System. *IEEE Trans Instrum Meas* 2015; 64: 873-887. DOI: 10.1109/TIM.2014.2362417.
42. Sohn H, Lim HJ, DeSimio MP, et al. Nonlinear ultrasonic wave modulation for online fatigue crack detection. *J Sound Vib* 2014; 333: 1473-1484. DOI: https://doi.org/10.1016/j.jsv.2013.10.032.
43. Zhao X, Gao H, Zhang G, et al. Active health monitoring of an aircraft wing with embedded piezoelectric sensor/actuator network: I. Defect detection, localization and growth monitoring. *Smart Mater Struct* 2007; 16: 1208.
44. Hong M, Mao Z, Todd MD, et al. Uncertainty quantification for acoustic nonlinearity parameter in Lamb wave-based prediction of barely visible impact damage in composites. *Mech Syst Signal Pr* 2017; 82: 448-460. DOI: 10.1016/j.ymssp.2016.05.035.
45. Chandrasekaran S, Sato N, Tölle F, et al. Fracture toughness and failure mechanism of graphene based epoxy composites. *Compos Sci Technol* 2014; 97: 90-99. DOI: 10.1016/j.compscitech.2014.03.014.
46. Jia J, Du X, Chen C, et al. 3D network graphene interlayer for excellent interlaminar toughness and strength in fiber reinforced composites. *Carbon* 2015; 95: 978-986. DOI:

10.1016/j.carbon.2015.09.001.